International Journal of Biological Macromolecules 153 (2020) 736–746

Contents lists available at ScienceDirect

International Journal of Biological Macromolecules

journal homepage: http://www.elsevier.com/locate/ijbiomac

Highly efficient multifunctional graphene/chitosan/magnetite nanocomposites for photocatalytic degradation of important dye molecules

Muthuchamy Maruthupandy [a,*], Thillaichidambaram Muneeswaran [a], Muthusamy Anand [b], Franck Quero [a,*]

[a] Laboratorio de Nanocelulosa y Biomateriales, Departamento de Ingeniería Química, Biotecnología y Materiales, Facultad de Ciencias Físicas y Matemáticas, Universidad de Chile, Avenida Beauchef 851, Santiago, Chile
[b] Department of Marine and Coastal Studies, Madurai Kamaraj University, Madurai 625 021, Tamil Nadu, India

ARTICLE INFO

Article history:
Received 22 January 2020
Received in revised form 4 March 2020
Accepted 6 March 2020
Available online 10 March 2020

Keywords:
Multifunctional graphene/chitosan/magnetite nanocomposites
Hydrothermal synthesis
Photocatalytic degradation

ABSTRACT

Multifunctional chitosan/magnetite (CS/Fe_3O_4) and graphene/chitosan/magnetite (Gr/CS/Fe_3O_4) nanocomposites (NCs) were synthesized using a simple hydrothermal method. The NCs were subsequently evaluated as magnetic photocatalysts towards the photodegradation of dye molecules that are detrimental to the environment. In the present study, sphere shaped Fe_3O_4 nanoparticles (NPs) were found to uniformly decorate CS and Gr surfaces. The synthesized Fe_3O_4 NPs, CS/Fe_3O_4 and Gr/CS/Fe_3O_4 NCs were characterized by powder X-ray diffraction, Fourier-transform infrared and Raman spectroscopy, thermogravimetric analysis, UV–visible diffuse reflectance and photoluminescence spectroscopy, and field emission scanning electron microscopy coupled with energy dispersive X-ray spectroscopy. The Gr/CS/Fe_3O_4 NCs showed 100% photocatalytic efficiency against rhodamine B (40 min), bromothymol blue (60 min), methylene blue (80 min) and methyl orange (100 min) compared to Fe_3O_4 NPs (100 min for Rh-B, 120 min for BTB, 160 min for MB and 180 min for MO) and CS/Fe_3O_4 NCs (90 min for Rh-B, 100 min for BTB, 140 min for MB and 150 min for MO). The photocatalytic irradiation efficiency of Fe_3O_4 NPs, CS/Fe_3O_4 and Gr/CS/Fe_3O_4 NCs, evaluated against visible light, was found to be significantly higher for Rh-B (100% within 40 min) compared to the other tested dyes.

1. Introduction

In recent years, the level of toxic chemical substances that end up in the environment has been increasing at an alarming level, threatening several forms of life on earth. Among them, dye molecules are important chemicals that damage the aquatic ecosystem [1]. These are carcinogenic in nature and cause mutations in invertebrates. Wastewater that originate from dye industries are dumped into aquatic ecosystem, which causes severe water pollution. Although a wide range of dye molecules are available, rhodamine-B (Rh-B), methylene blue (MB), methyl orange (MO), bromothymol blue (BMB) are still widely used in the chemical and medical industries. According to a very recent study, the level of these mutagenic and carcinogenic dye molecules is high in wastewater [2]. Hence, it is necessary to address this problem caused by these toxic dye molecules.

For the removal of dyes from wastewater, physical, chemical and biological techniques have been reported [3]. The traditional methods employed for the degradation of dyes have, however, several limitations including high cost, low efficiency, instability, high-energy consumption, among others. Currently, adsorption and catalysis processes are being investigated for the photodegradation of dyes, which have shown high potential to be used as alternative methods for sustainable removal of dyes from environmental water [4].

Nanocomposites (NCs) based on graphene (Gr), biopolymers including chitosan (CS) and magnetic particles have gained more attention owing to their potential to solve problems related to the biomedical and environmental sectors [5,6]. Gr is a thin, two-dimensional (2D) allotrope of carbon atoms bonded together in a repeating pattern of hexagons [7]. The hexagonal arrangements of carbon atoms provide many extraordinary characteristics to Gr, including transparency, lightweight, conductivity and mechanical strength [8]. Gr has been reported to be the strongest material in the world reported to date [9]. In addition, Gr has been reported to possess unique features such as high specific surface area, low cytotoxicity and good water stability [10]. Gr and Gr-based materials have shown tremendous potential for applications in medicine and life sciences, including imaging [11],

* Corresponding authors at: Laboratorio de Nanocelulosa y Biomateriales, Departamento de Ingeniería Química, Biotecnología y Materiales, Facultad de Ciencias Físicas y Matemáticas, Universidad de Chile, Av. Beauchef 851, Santiago, Chile.
E-mail addresses: mmaruthupandy@yahoo.in (M. Maruthupandy), fquero@ing.uchile.cl (F. Quero).

https://doi.org/10.1016/j.ijbiomac.2020.03.045
0141-8130/

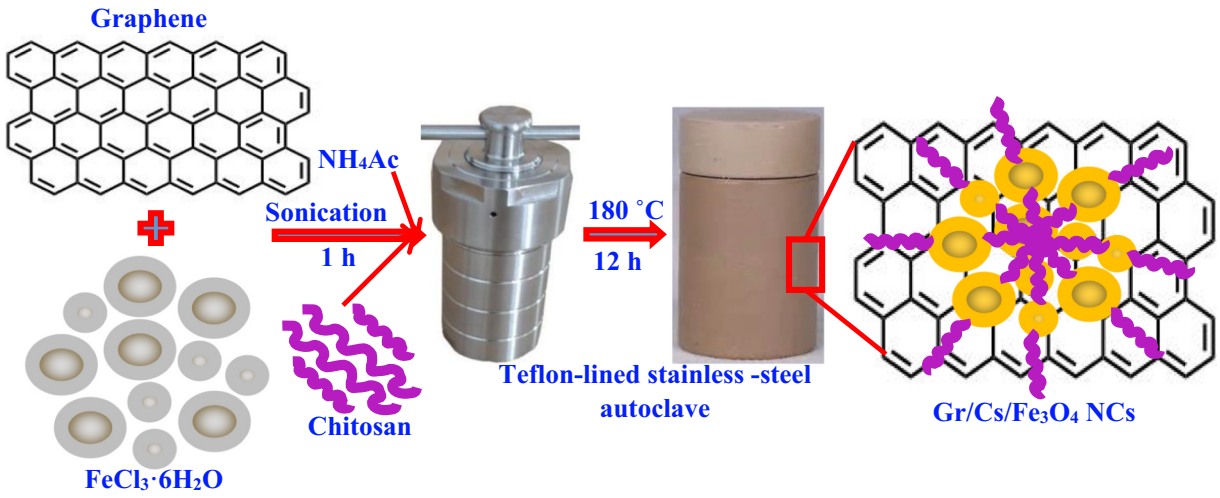

Scheme 1. Schematic representation illustrating the simple one-step synthesis of CS/Fe_3O_4 and Gr/Fe_3O_4/Cs NCs.

biosensors [12], drug delivery [13], photocatalysis [14] and antibacterial activity [15].

Gr and iron oxide nanoparticles (NPs) combined with biopolymers including CS have been attracting interests due to their relevance to be used for biomedical applications including drug delivery [16], resonance imaging (MRI) contrast agents [17], high gradient magnetic field separations [18], treatment of retinal detachment [19], biocatalysis [20] and magnetic bio-separations [21]. Owing to their biocompatibility and low toxicity, magnetite (Fe_3O_4) nanoparticles (NPs) are one of the most attractive candidates for use in clinical applications [22]. Other attractive features of Fe_3O_4 NPs for use in biomedical applications include their superparamagnetic behaviour at room

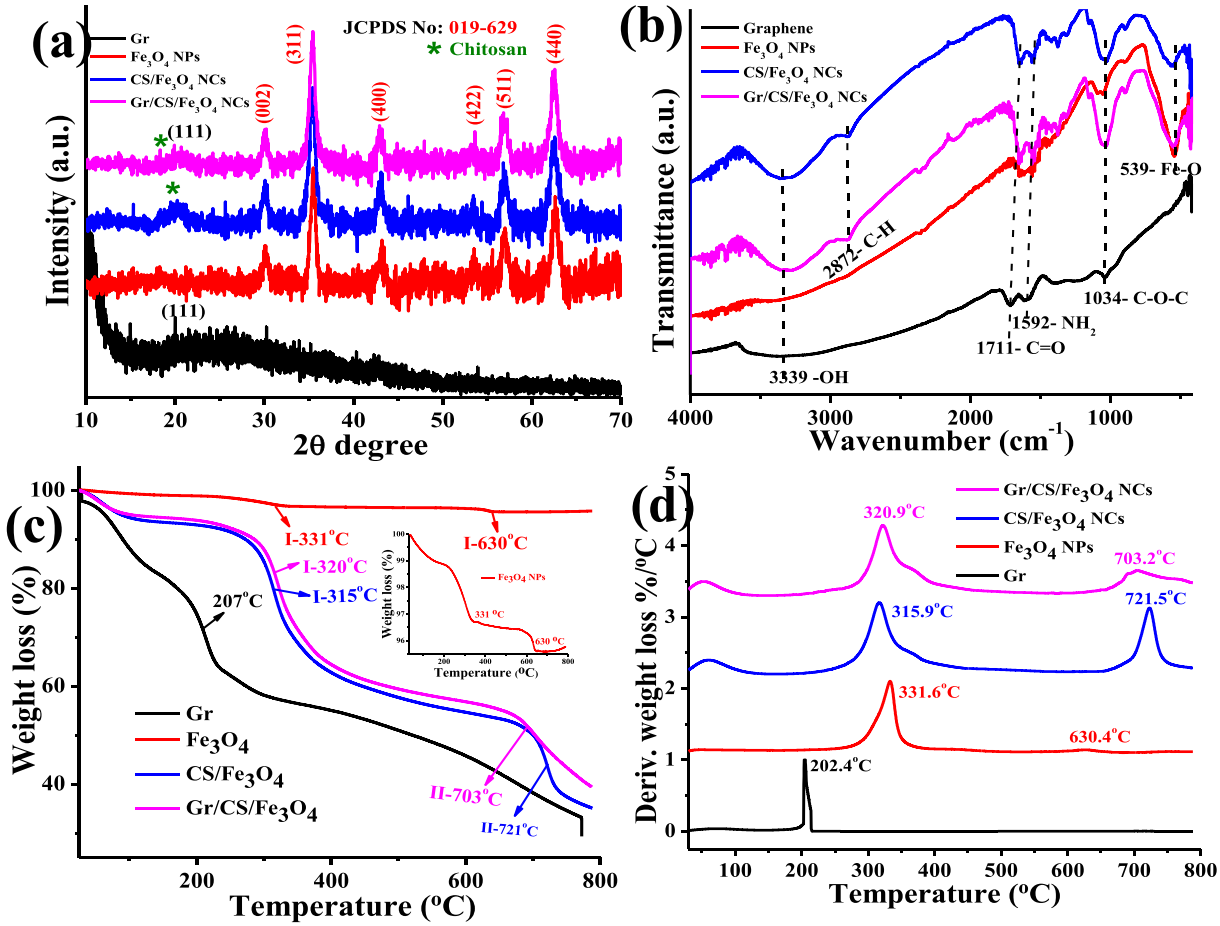

Fig. 1. (a) Powder XRD patterns obtained in the 2θ range of 10 to 70°, (b) FTIR spectra in the wavenumber range of 4000 to 400 cm^{-1} at a spectral resolution of 4 cm^{-1}, (c) TGA curves and (d) DTG analysis obtained from the first derivatives of the TGA curves for Gr, Fe_3O_4 NPs, CS/Fe_3O_4 NCs and Gr/CS/Fe_3O_4 NCs.

temperature as well as their charged surface, which are important characteristics that relate to their biological activity. Their initial surface charge is, however, not constant in the presence of biofilms, leading to Fe_3O_4 NPs with superparamagnetic behaviour with fairly similar surface charges in situ [23].

CS is a biological and biocompatible macromolecule that has been reported to improve the dispersion of iron oxide NPs [24]. Also, it has been reported to enhance the photocatalytic degradation efficiency of organic dyes [25]. In a previous study, graphene oxide (GO)/CS/Fe_3O_4 NCs was found to be relatively efficient at removing methylene blue (MB) molecules from wastewater. No other dye was, however, evaluated [26]. Preethi et al. evaluated the photocatalytic reduction of hexavalent chromium (Cr(VI)) using zinc oxide (ZnO), zinc oxide impregnated chitosan beads (ZCB) and chitosan/zinc oxide composite (CZC) under UV light irradiation [27]. Mahalingam and Ahn reported that GO-Fe_3O_4-NiO hybrid nanocomposites enriched the photocatalytic activity of methyl red and crystal violet dyes under visible light for industrial wastewater treatment [28]. Studies that focus on evaluating Gr/CS/Fe_3O_4 NCs as photocatalyst for a wide range of important dye molecules are scarce. These NCs obtained by hydrothermal synthesis could potentially result in much improved photocatalytic activity when compared to GO/CS/Fe_3O_4 NCs that were synthesized by a low yield co-precipitation method [16]. The main hypothesis of the work is to present an investigation where a simple and efficient hydrothermal method was utilized for the synthesis of CS/Fe_3O_4 and Gr/CS/Fe_3O_4 NCs. The obtained samples were characterized by powder X-ray diffraction (XRD), Fourier transform infrared spectroscopy (FTIR), thermogravimetric analysis (TGA), Raman spectroscopy, photoluminescence spectroscopy and scanning electron microscopy (SEM) coupled with energy-dispersive X-ray spectroscopy (EDX). The potential of these NCs for photocatalytic degradation of important dye molecules (Rh-B, BTB, MB and MO) was quantified against visible light by UV–visible spectrophotometry.

2. Material and methods

2.1. Materials

Graphite powder (99.95%), chitosan (M_w = 310,000–375,000 Da; degree of deacetylation >75%) and iron (III) chloride hexahydrate ($FeCl_3 \cdot 6H_2O$) were purchased from Sigma-Aldrich, Chile. 37 wt% hydrochloric acid (HCl), 98 wt% sulfuric acid (H_2SO_4), hydrogen peroxide (H_2O_2), potassium permanganate ($KMnO_4$), hydrazine hydrate (N_2H_4) and absolute ethanol were purchased from Merck, Chile. All chemicals were used as received without further purification. Deionized water (dH_2O) was used throughout this study.

2.2. Synthesis of graphene (Gr)

Graphite oxide was synthesized by using a modified Hummer's method [29]. Briefly, 1 g of graphite powder was added to 80 mL of H_2SO_4 and stirred in an ice bath. After 30 min, 6 g of $KMnO_4$ was slowly added to the previous solution and stirred. Then, the ice bath was replaced by an oil bath (30–35 °C) and the solution was stirred magnetically overnight. Then, 100 mL of dH_2O was slowly added and stirred for 30 min. A mixture of H_2O_2 (5 mL) and dH_2O (100 mL) was slowly added to the previous solution and stirred for 10 min. The solution was subsequently filtered using Whatman filter paper to recover the graphite oxide. The precipitate was subsequently washed (3–4 times) using HCl and then washed several times with dH_2O until neutral pH was reached. The synthesized graphite oxide was then dispersed in dH_2O and sonicated for 4 h to obtain graphene oxide (GO). The dried

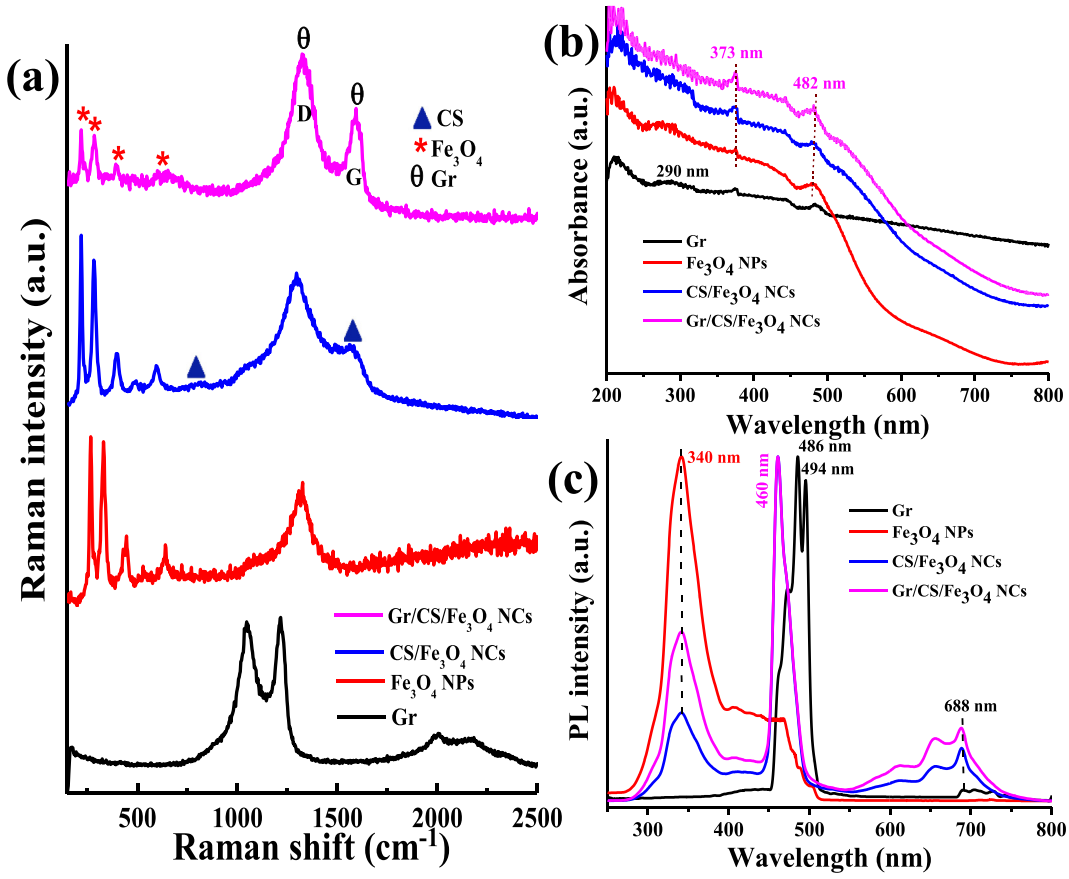

Fig. 2. (a) Raman spectra in the Raman shift range of 100 to 2000 cm^{-1}, (b) UV-DRS spectra wavelength range of 200 to 800 nm and (c) PL spectra wavelength range of 200 to 800 nm of Gr, Fe_3O_4 NPs, CS/Fe_3O_4 NCs and Gr/CS/Fe_3O_4 NCs.

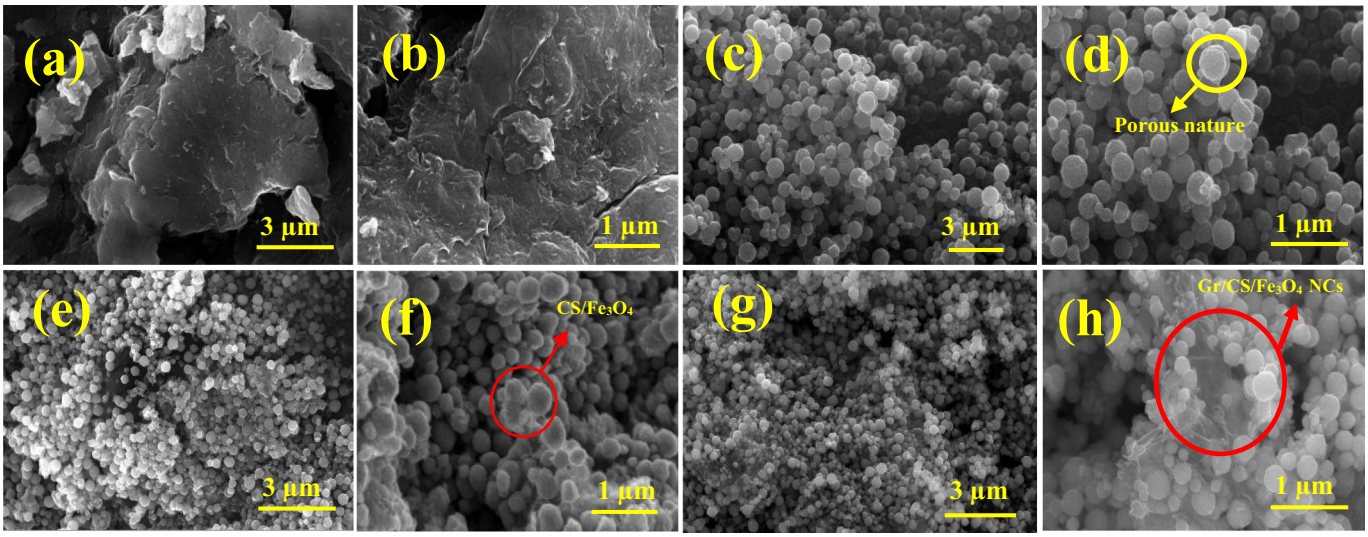

Fig. 3. Low and high magnification FE-SEM micrographs of (a, b) Gr, (c, d) Fe_3O_4 NPs, (e, f) CS/Fe_3O_4 NCs and (g, h) Gr/CS/Fe_3O_4 NCs.

GO powder was dispersed in 90 mL of dH_2O (10 mg/mL) and further sonicated for 30 min. Then, 30 µL of N_2H_4 was added to the solution and the resulting mixture was stirred for 3 h at 80 °C to obtain finally graphene (Gr).

2.3. Synthesis of Fe_3O_4 NPs, CS/Fe_3O_4 and Gr/CS/Fe_3O_4 NCs

Gr/CS/Fe_3O_4 NCs were synthesized as follows. Briefly, 13.6 mg of Gr and 0.68 g of $FeCl_3 \cdot 6H_2O$ were dissolved in 35 mL of ethylene glycol (EG) to form a homogeneous solution. A mixture of NH_4Ac (1.92 g) and chitosan (0.68 g) was subsequently added to the above suspension and dispersed for 1 h by sonication. Then, the resulting mixture was transferred into a Teflon-lined stainless-steel autoclave (40 mL), heated to 180 °C and kept at this temperature for 12 h. After cooling down to room temperature, the obtained products were washed with dH_2O and ethanol and then dried in a vacuum at 65 °C for 12 h. For comparison, Fe_3O_4 NPs and CS/Fe_3O_4 NCs were prepared under the same experimental conditions, without the use of CS and Gr, and Gr, respectively.

2.4. Characterization of Fe_3O_4 NPs, CS/Fe_3O_4 and Gr/CS/Fe_3O_4 NCs

Powder XRD patterns of the synthesized samples were recorded using a PANalytical X'Pert Pro diffractometer equipped with Cu-K_α radiation ($\lambda = 1.54178$ Å). FTIR spectra were recorded using a Thermo

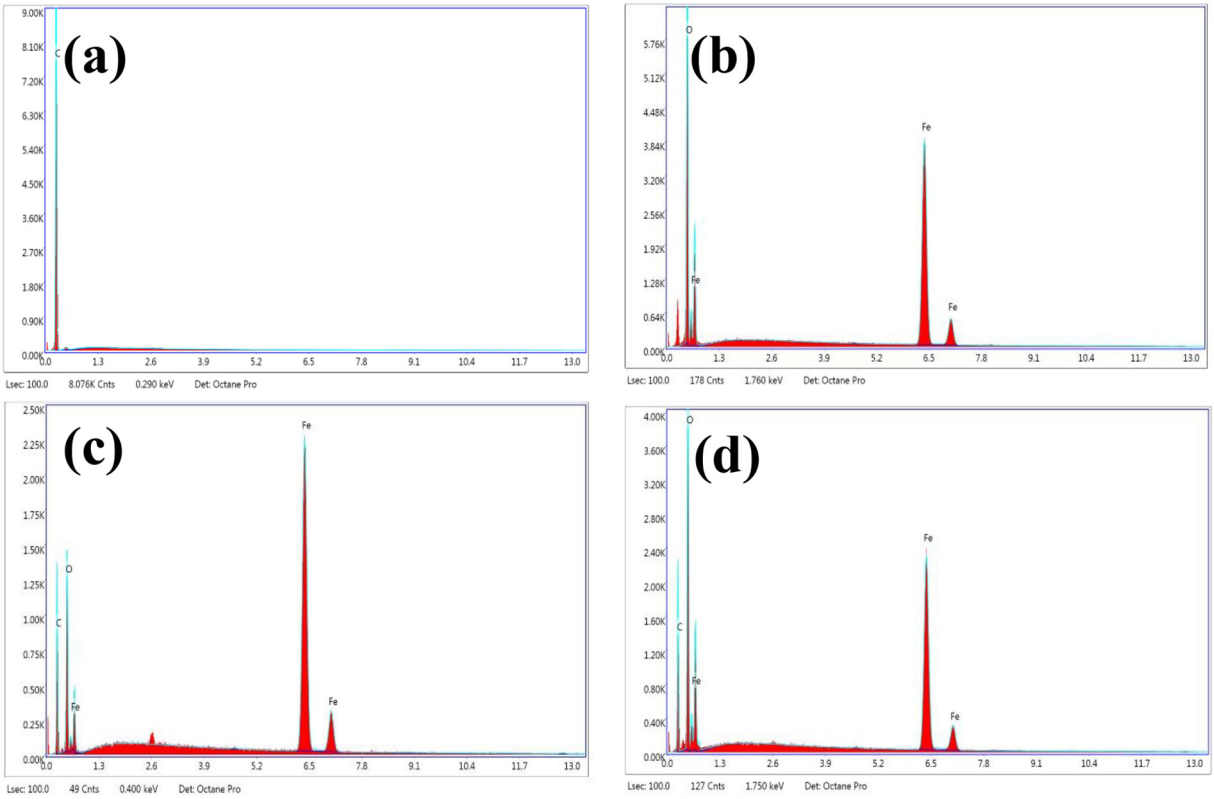

Fig. 4. EDX analysis of (a) Gr, (b) Fe_3O_4 NPs, (c) CS/Fe_3O_4 NCs and (d) Gr/CS/Fe_3O_4 NCs.

Scientific Nicolet iS10 spectrometer in the wavenumber range of 4000 to 400 cm^{-1} at a spectral resolution of 4 cm^{-1}. TGA analysis (TA, Q50) was performed using an air flow of 40 mL min^{-1} at a heating rate of 20 °C min^{-1} from 30 up to 800 °C. DTGA curves were obtained from the first derivatives of the TGA curves as a function of temperature. The structural morphology and chemical elemental analysis of the samples were assessed by scanning electron microscope (FESEM, Quanta FEG250) coupled with energy-dispersive X-ray spectroscopy (EDX, Ametax, Z1 analyser Z230). Raman spectra were obtained at room temperature in the Raman shift range of 100 to 2000 cm^{-1} using a Raman spectrometer (Alpha 300, Witec, Germany) equipped with an optical microscope and a laser having a wavelength of ~532 nm. Solid-state photoluminescence (PL) spectra were acquired at room temperature using a fluorimeter (Perkin Elmer, LS 55). The UV–visible diffuse reflectance spectra (UV–Vis DRS) were recorded using a spectrophotometer (Shimadzu 2600).

2.5. Photocatalytic activity

The photocatalytic activity of CS/Fe_3O_4 and $Gr/CS/Fe_3O_4$ NCs against Rh-B, BTB, MB and MO dyes was monitored in the visible light range using a UV–visible spectrophotometer (Perkin Elmer, Lambda 11). In each experiment, ~50 mg of photocatalyst was dispersed in 100 mL of Rh-B, BTB, MB and MO aqueous solutions (1×10^{-5} M). The suspension was then magnetically stirred under dark condition for 30 min. The solution was subsequently transferred to a flask and exposed to visible light radiation at a regular interval time of 10 min. The photocatalytic degradation process was monitored by following intensity changes of absorption peaks located in the visible light range at wavelength positions of ~550, 660, 430 and 465 nm corresponding to Rh-B, BTB, MB and MO, respectively. Each test was conducted in triplicate.

3. Results and discussion

3.1. Characterization of CS/Fe_3O_4 and $Gr/CS/Fe_3O_4$ NCs

Scheme 1 reports an illustration of the single-step hydrothermal method used to synthesis CS/Fe_3O_4 and $Gr/CS/Fe_3O_4$ NCs. These were subsequently characterized as follows. The powder XRD patterns of Gr, Fe_3O_4 NPs, CS/Fe_3O_4 and $Gr/CS/Fe_3O_4$ NCs are shown in Fig. 1a. The XRD pattern of Gr displays a strong diffraction peak located at a diffraction angle position of $2\theta = 21.6°$. This diffraction peak corresponds to the (111) plane of Gr. The XRD pattern of Fe_3O_4 NPs shows diffraction peaks located at diffraction angle values of 2θ ~30°, 35°, 43°, 53°, 56° and 62°. These correspond to the diffraction planes of (102), (311), (400), (422), (511) and (440), respectively. The XRD pattern of Fe_3O_4 NPs further shows that the NPs are spherical and the related planes highly agree with the JCPDS Card No: 019-629 [30]. In the diffraction pattern corresponding to CS/Fe_3O_4 NCs, one can clearly observed the diffraction peaks occurring due to the presence of Fe_3O_4 NPs [31]. The powder XRD pattern corresponding to the CS/Fe_3O_4 NCs confirms the presence of CS due to the presence of a diffraction peak located at a

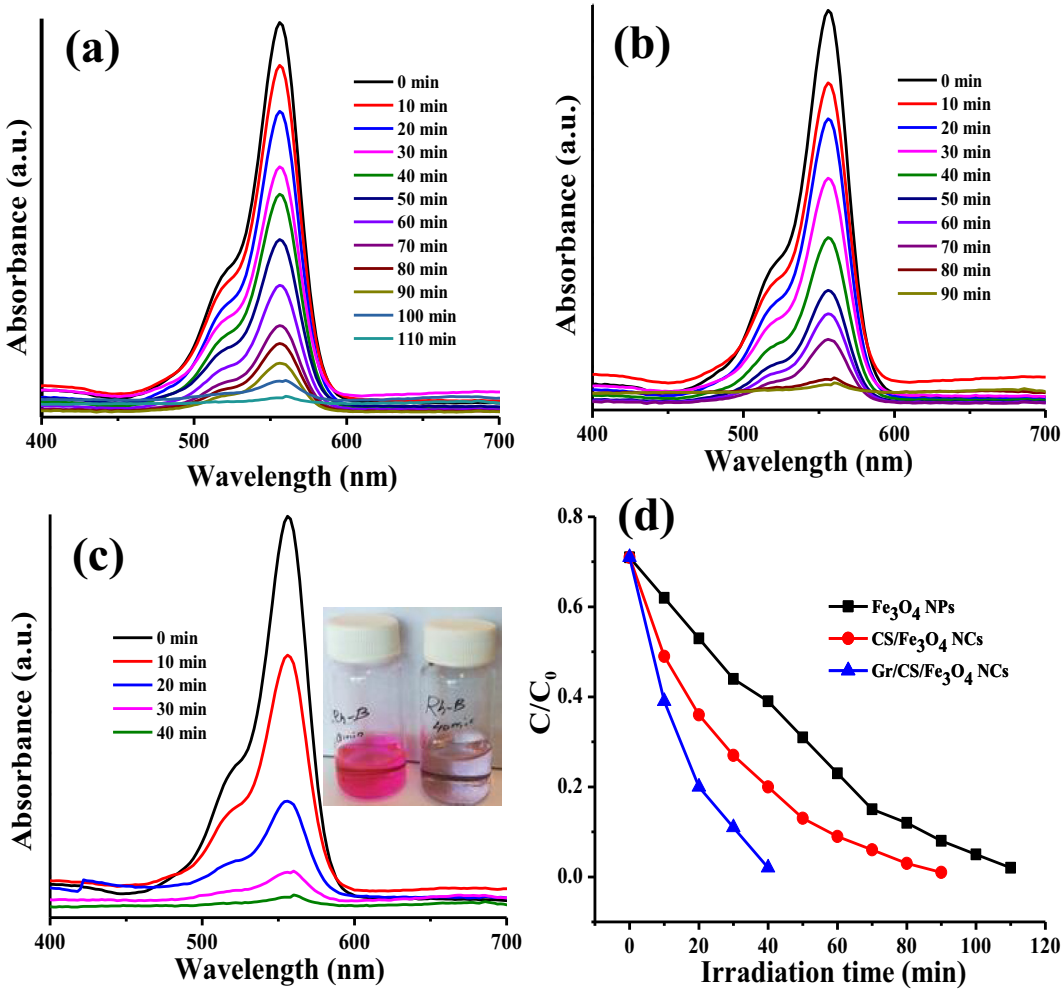

Fig. 5. Time dependent UV–visible absorption spectra obtained in the wavelength range of 400 to 700 nm for Rh-B treated with (a) Fe_3O_4 NPs, (b) CS/Fe_3O_4 NCs, (c) $Gr/CS/Fe_3O_4$ NCs and (d) photocatalytic degradation of Rh-B in the presence of Fe_3O_4 NPs, CS/Fe_3O_4 NCs and $Gr/CS/Fe_3O_4$ NCs.

diffraction angle position 2θ of ~19°. This suggests that the CS macromolecules are bounded to the surface of Fe_3O_4 NPs. The powder XRD pattern of Gr/CS/Fe_3O_4 NCs displays the typical diffraction peaks of Fe_3O_4 NPs, CS and Gr. One can observe that the diffraction peak corresponding to the crystalline phase of CS is slightly shifted from a diffraction angle 2θ value of ~19° to 18°. The intensity of this peak is found to decrease upon the addition of Gr into the CS/Fe_3O_4 NCs. The crystallinity of CS is determined by the intramolecular and intermolecular hydrogen bonds of its tertiary structure [32,33]. Researchers found that the crystallization of CS is enhanced by the presence of hydrogen bond breaking compounds [34,35]. In a previous study, Gr was found to affect the crystallization of CS, acting as nucleating agent [36,37]. Changes in hydrogen bonding, however, can also lead to a change of CS crystallinity. The diffraction peaks corresponding to Gr, CS, and Fe_3O_4 are clearly seen in the XRD pattern of Gr/CS/Fe_3O_4 NCs. This suggested that CS and Fe_3O_4 NPs were successfully deposited onto the Gr surface (Scheme 1). The powder XRD pattern does not show any other additional peaks other than the ones corresponding to Gr, CS, and Fe_3O_4. This indicated that the CS/Fe_3O_4 and Gr/CS/Fe_3O_4 NCs are free of crystalline or semi-crystalline impurities.

The FTIR spectra of Gr, Fe_3O_4 NPs, CS/Fe_3O_4 and Gr/CS/Fe_3O_4 NCs are shown in Fig. 1b. The FTIR spectrum of Gr exhibits characteristic absorption peaks located at a wavenumber of ~3339 cm^{-1}. This peak is related to the vibrational motions of

OH moieties. Two other absorption peaks are located at wavenumber positions of ~1711 and 1592 cm^{-1}. These are related to the vibrational motions of C═O and NH_2 groups, respectively. The peak located at a wavenumber position of ~1034 cm^{-1} corresponds to the vibrational motions of C—O—C [38]. The FTIR spectrum of Fe_3O_4 NPs shows characteristics absorption peaks related to the vibrational motions of OH groups. These peaks were found to be located at wavenumber positions of ~3362 and 1586 cm^{-1}. A relatively strong absorption peak associated to the vibrational motions of Fe—O bonds was found to occur at a wavenumber position of ~539 cm^{-1} [39]. The FTIR spectrum corresponding to CS/Fe_3O_4 NCs is similar to the spectrum observed for Fe_3O_4 NPs. One can observe, however, a slight shift and increased intensity for the peak located at a wavenumber position of ~3270 cm^{-1} that relates to the vibrational motions of OH moieties. The peaks located at wavenumber positions of ~1711, 1592 and 539 cm^{-1}, related to the vibrational motions of C—H, C═O, C═O, NH_2 and Fe—O groups, are also observed as reported for the FTIR spectrum of Fe_3O_4 NPs. One can also observe that the intensity of the absorption peak located at a wavenumber position of ~1034 cm^{-1}, corresponding to the vibrational motions of C—O—C, increases in the case of CS/Fe_3O_4 NCs. An absorption peak occurring due to the stretching motions of C—H moieties and located at a wavenumber position of ~2872 cm^{-1} appeared only in the spectrum corresponding to CS/Fe_3O_4 NCs, very likely due to presence of CS in the NCs. Comparable absorption peaks corresponding to the vibrational motions of O—H, C—H, C═O, C═O, —NH_2 and C—O—C moieties are observed in the spectrum of Gr/CS/Fe_3O_4 NCs, similarly to the CS/Fe_3O_4 NCs spectrum. When compared to the spectrum of CS/Fe_3O_4 NCs, one can observe that the intensity of the absorption peak located

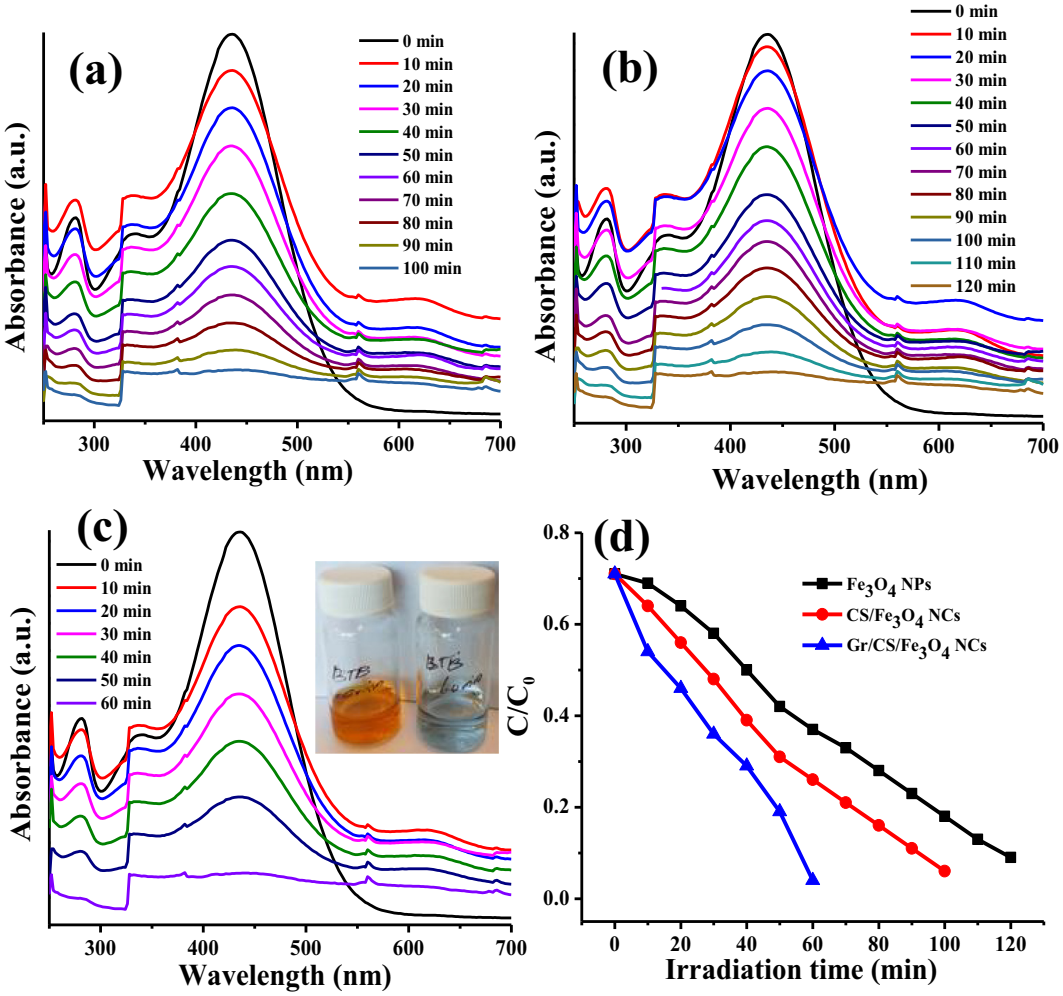

Fig. 6. Time dependent UV–visible absorption spectra obtained in the wavelength range of 200 to 700 nm for BTB treated with (a) Fe_3O_4 NPs, (b) CS/Fe_3O_4 NCs, (c) Gr/CS/Fe_3O_4 NCs and (d) photocatalytic degradation of BTB in the presence of Fe_3O_4 NPs, CS/Fe_3O_4 NCs and Gr/CS/Fe_3O_4 NCs.

at a wavenumber position of ~539 cm^{-1} related to the vibrational motions of Fe—O bonds increases in the Gr/CS/Fe_3O_4 NCs spectrum, possibility due to the addition of Gr. This change in peak intensity suggests the formation of CS/Fe_3O_4 NCs onto the surface of Gr, following its partial reduction [40–43].

TGA of Gr, Fe_3O_4 NPs, CS/Fe_3O_4 NCs and Gr/CS/Fe_3O_4 NCs was performed to study their thermal stability and binding conformation ability of Fe_3O_4 NPs, CS/Fe_3O_4 NCs onto the surface of Gr. Their corresponding spectra are reported in Fig. 1c. The TGA curve of Gr showed a typical weight loss upon increasing temperature. The weight loss was found to be relatively small, which suggests that the Gr material is highly pure. The weight loss occurring at ~207 °C can be attributed to the decomposition of functional labile oxygen group present at the surface of Gr [44]. The total weight loss of Gr was found to be ~67%. The TGA curve of Fe_3O_4 NPs showed two weight loss stages with cumulative temperature. The first stage of weight loss is reached at ~304 °C with a corresponding weight loss of ~3% probably due to the loss of free water. The second weight loss was found to occur at ~633 °C with a corresponding weight loss of ~1.1%, which can be attributed to the loss of more tightly bound water molecules. The TGA curve of CS/Fe_3O_4 NCs showed two stages of weight loss upon increasing temperature. The first weight loss occurred at ~315 °C due to the thermal decomposition of amine and —CH_2OH groups present along the molecular structure of CS [45]. The second weight loss was found to occur at ~721 °C. This can be attributed to the thermal degradation of Fe_3O_4 NPs [46]. A total weight loss of ~65% was observed for CS/Fe_3O_4 NCs. Likewise, the TGA curve of Gr/CS/Fe_3O_4 NCs shows a two stage weight loss. The temperature at which these weight loss stages occurred are shifted to higher temperature, very likely due to the presence of Gr. When compared to the total weight loss of CS/Fe_3O_4 NCs (~65%), the total weight loss for Gr/CS/Fe_3O_4 NCs was found to be ~62%. This suggests that the synthesized Gr/CS/Fe_3O_4 NCs possess higher thermal stability compared to Fe_3O_4 NPs and CS/Fe_3O_4 NCs at temperatures close to 720 °C. At lower temperatures, no significant difference was observed when comparing CS/Fe_3O_4 NCs and Gr/CS/Fe_3O_4 NCs.

DTGA curves of Gr, Fe_3O_4 NPs, CS/Fe_3O_4 NCs and Gr/CS/Fe_3O_4 NCs are reported in Fig. 1d. These confirm that polar groups interact with water through hydrogen bonding. The two peaks of the DTGA curves of Gr confirmed that the thermal degradation of organic compounds occurred at ~202 °C. The DTGA curve of Fe_3O_4 NPs shows degradation temperature peaks at ~331 °C and 630 °C, corresponding to the thermal degradation of amine and primary alcohol as well as their carbonization temperature, respectively. CS/Fe_3O_4 NCs shows DTGA temperature peaks located at ~59 °C, 315 °C, 721 °C, which correspond to the thermal degradation of amine and —CH_2OH present within the molecular structure of CS and the thermal degradation of Fe_3O_4 NPs. Furthermore, this suggests that the arrangement of CS onto the surface of Fe_3O_4 NPs decreases their thermal stability [47–49]. The DTGA curve of Gr/CS/Fe_3O_4 NCs depicts that the thermal degradation peaks are similar to the peaks of CS/Fe_3O_4 NCs. These, however, slightly shifted to lower temperatures. As a result, Gr/CS/Fe_3O_4 NCs that possess relatively good thermal stability were successfully synthesized.

Raman spectroscopy is a relevant technique to provide information about the chemical structure of carbon-based materials, including Gr [50]. Raman spectra of the Gr, Fe_3O_4 NPs, CS/Fe_3O_4 NCs and Gr/CS/Fe_3O_4 NCs are reported in Fig. 2. The spectrum of Gr sheet shows the

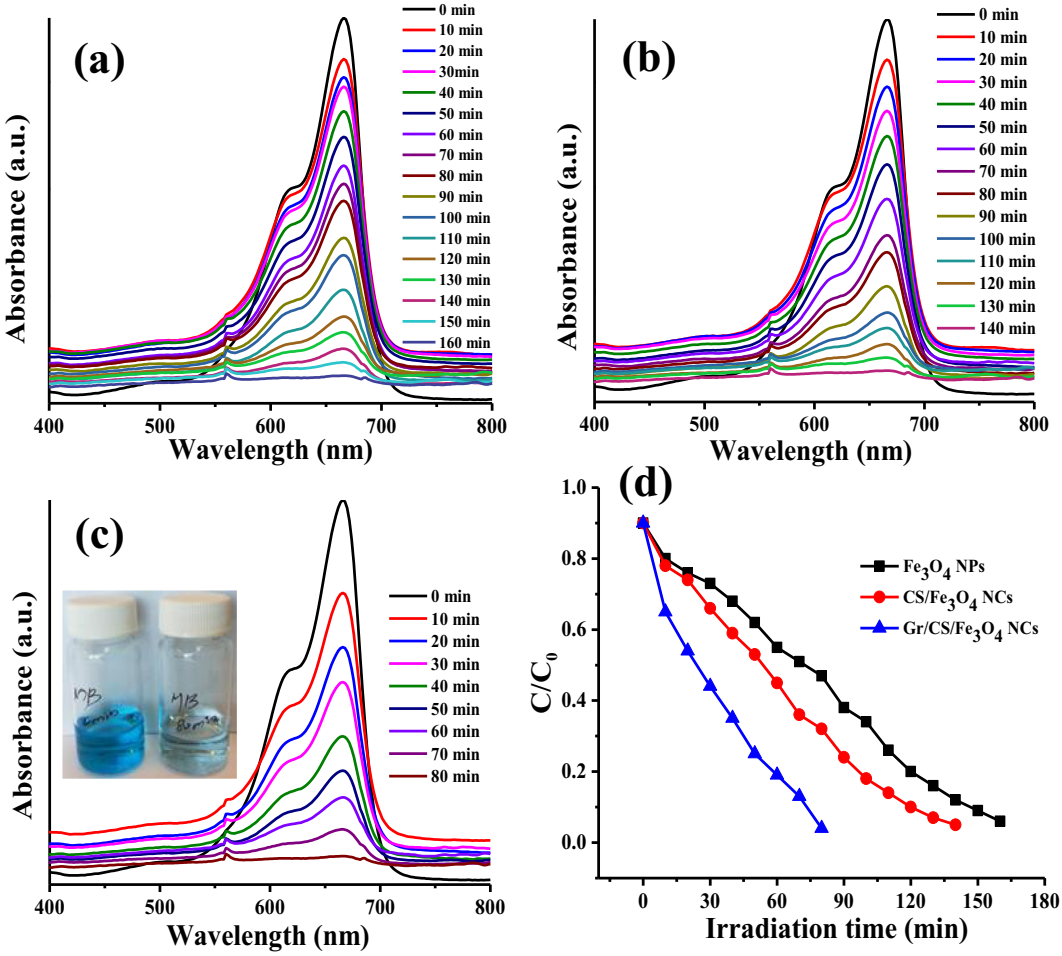

Fig. 7. Time dependent UV–visible absorption spectra obtained in the wavelength range of 400 to 800 nm for MB treated with (a) Fe_3O_4 NPs, (b) CS/Fe_3O_4 NCs, (c) Gr/CS/Fe_3O_4 NCs and (d) photocatalytic degradation of MB in the presence of Fe_3O_4 NPs, CS/Fe_3O_4 NCs and Gr/CS/Fe_3O_4 NCs.

presence of the typical D band located at a Raman shift position of ~1050 cm^{-1} and the typical G band located at a Raman shift position of ~1219 cm^{-1}. These bands may be attributed to the sp3 defects and in-plane vibrations of sp2 bonds that link together carbon atoms, respectively [51]. The intensity of the D and G bands provides information on the morphological alterations of carbon-based materials [40]. The Raman bands corresponding to Fe_3O_4 NPs are located at Raman shift positions of ~215, 287, 393, 602 and 1300 cm^{-1}. These are occurring due to the typical vibrational modes of Fe_3O_4 NPs. The peak observed at ~1300 cm^{-1} confirms the presence of magnetite [52]. With the exception of the presence of an additional band observed at a Raman shift position of ~1581 cm^{-1}, all the Raman bands of CS/Fe_3O_4 NCs are similar to the Raman bands of Fe_3O_4 NPs. The observation of this additional band may be attributed to the presence of CS. The Raman spectrum of Gr/CS/Fe_3O_4 NCs showed, however, a slight increase in intensity and shift towards higher wavenumber for the D and G bands, which Raman shift positions were found to be ~1324 and 1592 cm^{-1}, respectively. Moreover, the intensity of the Raman bands corresponding to Fe_3O_4 NPs was found to decrease. The Raman band corresponding to CS could not be detected for CS/Fe_3O_4 NCs, possibly due to the presence of Gr. The intensity of the D band, however, is higher when compared to the G band for the Gr/CS/Fe_3O_4 NCs indicate the occurrence of sp3 defects during the functionalization procedure of the exfoliated Gr [53].

The UV–Vis diffuse reflectance spectra of Gr, Fe_3O_4 NPs, CS/Fe_3O_4 NCs and Gr/CS/Fe_3O_4 NCs are shown in Fig. 2b. The spectra of Gr and Fe_3O_4 NPs show absorption bands in the UV range positioned at wavelength of ~290 nm and ~373, ~482 nm, respectively. A slight blue shift from ~376 nm to ~373 nm and red shift from ~478 nm to ~482 nm can be observed upon the addition of CS and Gr in the Fe_3O_4 NPs, as depicted by the spectra of CS/Fe_3O_4 NCs and Gr/CS/Fe_3O_4 NCs. This may suggest that CS/Fe_3O_4 NCs are located onto the surface of Gr sheets. The PL spectra of the Gr, Fe_3O_4 NPs, CS/Fe_3O_4 NCs and Gr/CS/Fe_3O_4 NCs are reported in Fig. 2c. The PL spectrum of CS/Fe_3O_4 NCs and Gr/CS/Fe_3O_4 NCs clearly show an extensive yellow-green emission peak with a relatively broad position ranging from ~440 to ~505 nm centred at ~460 nm. This has been reported to be mostly occurring due to oxygen space in Fe_3O_4 NPs arrangement [54]. The PL spectrum of Gr/CS/Fe_3O_4 NCs was found to shift towards a lower wavelength when compared to pure Fe_3O_4 NPs. This has been reported to be due to the excellent electron contributing nature of Fe_3O_4 NPs and outstanding electron accepting nature of Gr. The decreased intensity of Fe_3O_4 NPs could be attributed to electron transfer from Fe_3O_4 NPs to Gr [55]. The remarkable electron free movement has been found to reduce the recombination of photo-created electron–hole pairs [56]. Due this special ability, Gr/CS/Fe_3O_4 NCs could potentially show better photocatalytic action than Fe_3O_4 NPs and CS/Fe_3O_4 NCs.

The surface morphology of Gr, Fe_3O_4 NPs, CS/Fe_3O_4 NCs and Gr/CS/Fe_3O_4 NCs were examined by FE-SEM as shown in Fig. 3. Fig. 3a, b show the surface morphology of Gr, which appears as a sheet-like structure. SEM images of Fe_3O_4 NPs show sphere-like morphology (Fig. 3c, d) with homogeneous surface morphology. Similarly, CS/Fe_3O_4 NCs also show a sphere-like morphology with their surface coated with CS (Fig. 3e, f). The Fe_3O_4 NPs present in the CS/Fe_3O_4 NCs are comparatively smaller in size compared to the Fe_3O_4 NPs obtain without CS. They also seem to possess a smoother surface, possibly due to addition CS onto their surface (Fig. 3f). The Gr/CS/Fe_3O_4 NCs were found to possess a

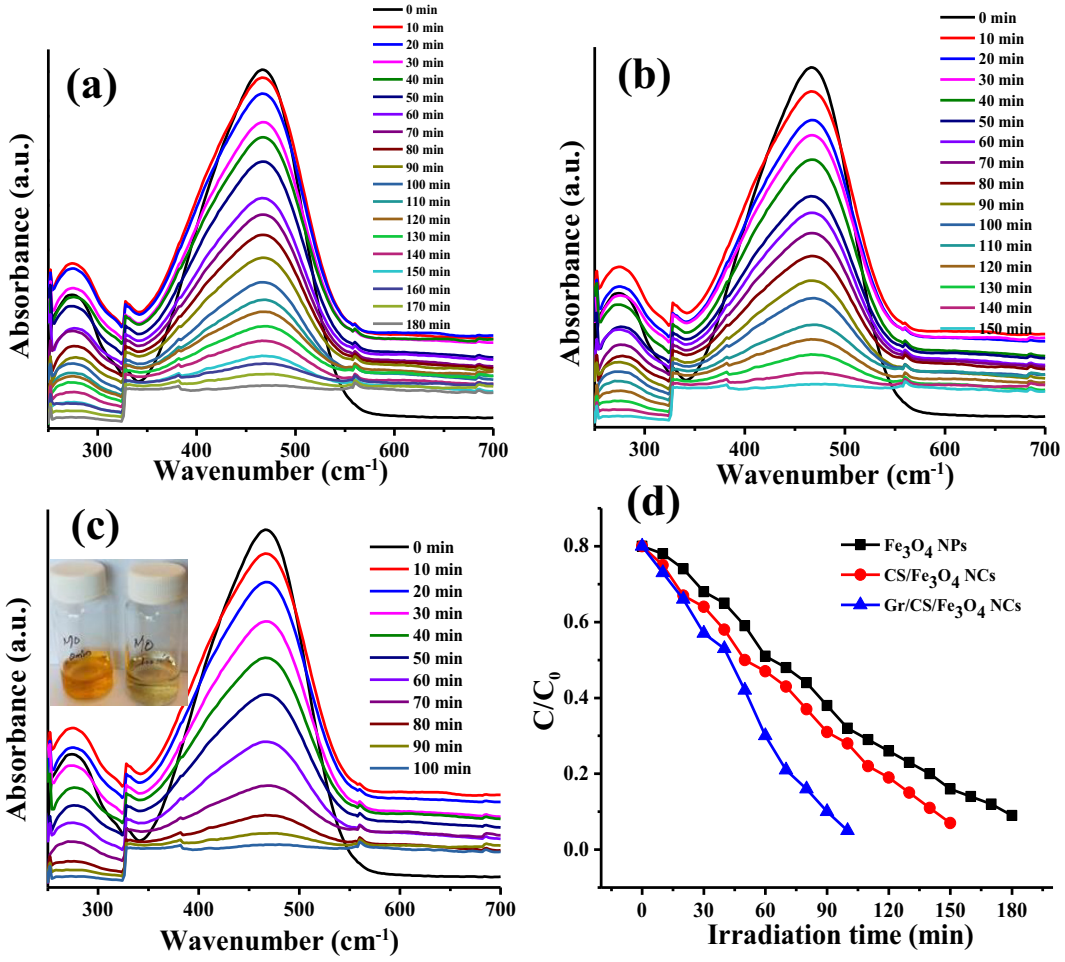

Fig. 8. Time dependent UV–visible absorption spectra obtained in the wavelength range of 200 to 700 nm for MO treated with (a) Fe_3O_4 NPs, (b) CS/Fe_3O_4 NCs, (c) Gr/CS/Fe_3O_4 NCs and (d) photocatalytic degradation of MO in the presence of Fe_3O_4 NPs, CS/Fe_3O_4 NCs and Gr/CS/Fe_3O_4 NCs.

similar morphology as CS/Fe_3O_4 NCs located at the surface of Gr sheets (Fig. 3g, h). Fig. 3h shows very clearly that CS/Fe_3O_4 NCs coat the surface of Gr sheets. Additionally, CS/Fe_3O_4 NPs seem to coat both sides of Gr sheets due to the occurrence of hydroxyl and carboxylic functional groups on both sides of the Gr sheets [57]. Another interesting observation is the surface roughness of the Fe_3O_4 NPs, which might contribute to increasing specific surface area and as a result could favour their adsorption behaviour [58]. The present study, however, do not provide direct evidence for this.

The chemical composition of the synthesized Gr, Fe_3O_4 NPs, CS/Fe_3O_4 NCs and Gr/CS/Fe_3O_4 NCs was assessed by EDX spectroscopy. The corresponding spectra are displayed in Fig. 4a–d. The EDX spectrum of Gr sheet suggests a chemical composition of 100% of atomic mass of carbon (C) (Fig. 4a). From Fig. 4b, it is clear that Fe_3O_4 NPs are constituted of 43.16% of oxygen (O) and 56.84% of iron (Fe). CS/Fe_3O_4 NCs were found to possess 30.06% of C, 23.38% of O and 46.55% of Fe (Fig. 4c) and the Gr/CS/Fe_3O_4 NCs 41.07% of C, 18.43% of O and 40.05% of Fe (Fig. 4d). The synthesized Gr, Fe_3O_4 NPs, CS/Fe_3O_4 NCs were found to be free from additional elemental impurities, suggesting that high purity materials were obtained through this simple hydrothermal synthesis method.

3.2. Photocatalytic activity

The efficiency of the synthesized Fe_3O_4 NPs, CS/Fe_3O_4 NCs and Gr/CS/Fe_3O_4 NCs towards the photocatalytic degradation of Rh-B, BTB, MB, and MO dye molecules was assessed in aqueous conditions against visible light. The spectrum of blank samples that contain individual Rh-B, BTB, MB, and MO dyes show absorption peak in the visible region located at wavelength of ~665, 465, 435 and 555 nm. The photocatalytic degradation of Rh-B, BTB, MB, and MO dye molecules in solution in the presence of synthesized Fe_3O_4 NPs, CS/Fe_3O_4 NCs and Gr/CS/Fe_3O_4 NCs was evaluated for 24 h at 15 min interval. It is obvious from the results that the intensity of the absorption peak of Rh-B, BTB, MB, and MO dye molecules decreased upon increasing irradiation time. The time requirement for the complete degradation of these dyes is, however, different.

Particularly, 100% of Rh-B dye molecule was degraded at irradiation times of 110, 90, 40 min in the presence of Fe_3O_4 NPs, CS/Fe_3O_4 NCs and Gr/CS/Fe_3O_4 NCs, respectively (Fig. 5a–c). Fe_3O_4 NPs, CS/Fe_3O_4 NCs and Gr/CS/Fe_3O_4 NCs fully degraded the BTB dye molecules at respective irradiation times of 120, 100, 60 min (Fig. 6a–c). These removed the MB dye molecules at irradiation times of 160, 140, 80 min, respectively (Fig. 7a–c). Fe_3O_4 NPs, CS/Fe_3O_4 NCs and Gr/CS/Fe_3O_4 NCs, however, took more prolonged time to degrade the MO dye molecules and their corresponding irradiation times are 180, 150, 100 min (Fig. 8a–c).

The corresponding images of photocatalytic degradation of Rh-B, BTB, MB, and MO dye molecules in the presence of Fe_3O_4 NPs, CS/Fe_3O_4 NCs and Gr/CS/Fe_3O_4 NCs under visible light irradiation are shown in Figs. 5d, 6d, 7d and 8d. The synthesized Gr/CS/Fe_3O_4 NCs were found to be twice more efficient at degrading completely all tested dyes compared to CS/Fe_3O_4 NCs and Fe_3O_4 NPs. Moreover, the photocatalytic degradation efficiency rate was found to decrease in the following order Rh-B > BTB > MB > MO in the presence of Fe_3O_4 NPs, CS/Fe_3O_4 NCs and Gr/CS/Fe_3O_4 NCs. It is possible that the CS/Fe_3O_4 NCs decorated on both sides of Gr sheets may have increased their specific surface area, which resulted in enhanced degradation of dye molecules. No direct evidence for this is, however, provided in the present study. The composition of the synthesized NCs possesses a majority of Fe(II) that can easily capture dye molecules and act as major catalytic specie in the photocatalytic reactions. Furthermore, the —OH radicals produced during the reaction may have positively influenced the degradation process. The negatively charged surface of Gr/CS/Fe_3O_4 NCs may reduce the negatively charged of the dye molecules, leading to an increased photocatalytic removal efficiency.

The good photocatalytic behaviour may be attributed to the conductive bonding of CS/Fe_3O_4 NCs on the Gr, which may lower the recombination of photocreated electron–gap pairs. This mechanism may be responsible for the enhanced degrading efficiency of Gr/CS/Fe_3O_4 NCs compared to Fe_3O_4 NPs, CS/Fe_3O_4 NCs. During the photocatalytic process, the dyes were transformed into reactive, unstable intermediates and mineralized to colourless compounds. Overall, the Gr/CS/Fe_3O_4 NCs required 40 min (Rh-B), 60 min (BTB), 80 min (MB) and 100 min (MO) for their complete degradation. The growing order of the efficiency of the complete removal of dye are Fe_3O_4 NPs < CS/Fe_3O_4 NCs < Gr/CS/Fe_3O_4 NCs. Electron–hole pairs in the excited Fe_3O_4 could be efficiently detached to enable an effective change into photo-induced electrons from Gr sheet to Fe_3O_4 NPs [59]. This essential electron transfer mechanism may play a vital role in the elimination of these dye molecules [60]. The efficiency of the photocatalytic response depends on the effectiveness of the adsorption of unprocessed organic impurities on the catalysts and the route of excruciating photocreated electron–hole pairs [61]. As a result, the enhanced photocatalytic activity of Gr/CS/Fe_3O_4 NCs could play an important role to solve dye related environmental problems.

Based on our results, some of the works reported previously in the literature and related to our studies are discussed. The photocatalytic degradation efficiency of Fe_3O_4/GO nanocomposites against rhodamine-B was found to be 93.5% at an exposure time of 190 min [62]. The photocatalytic degradation of Fe_3O_4/rGO nanocomposites against methylene blue and Rh-B were found to be 99% and 95% at exposure times of 90 and 120 min under direct sunlight irradiation [63]. Adsorption capacity (not based on photocatalysis) for methylene blue dye molecule was 98% using Gr/Fe_3O_4/CS nanocomposites during 90 min irradiation [14]. Tran et al. documented the photocatalytic decolourization of methylene blue dye molecules using GO/CS/Fe_3O_4 obtained by a co-precipitation method as adsorbent [16]. All samples were converted colourless after 40 min. This demonstrated the importance for the presence of GO to improve adsorption ability of GO/CS/Fe_3O_4 nanocomposites. Mahalingama and Ahn established that the photocatalytic efficiency of rGO–Fe_3O_4–NiO hybrid nanocomposite against methyl red and crystal violet dye molecules was 87% within 300 min under visible light irradiation [28]. As a result, the Gr/Cs/Fe_3O_4 NCs synthesized in the present study possess a very efficient photocatalytic activity against a wide range of dye molecules, demonstrating their relevance for environmental remediation application.

4. Conclusions

Fe_3O_4 NPs, CS/Fe_3O_4 NCs and Gr/CS/Fe_3O_4 NCs were synthesized via a hydrothermal method. The characterization of Gr/CS/Fe_3O_4 NCs suggested a moderately uniform distribution of CS-coated Fe_3O_4 NPs located onto the surface of graphene sheet. Powder XRD diffractograms and Raman spectra indicate a strong assembly between CS, Fe_3O_4 NPs and Gr sheet in the final NCs. FE-SEM micrographs showed that the synthesized Fe_3O_4 NPs, CS/Fe_3O_4 NCs and Gr/CS/Fe_3O_4 NCs possess sphered Fe_3O_4 NPs uniformly dispersed at their surface. Gr/CS/Fe_3O_4 NCs were found to possess multifunctional photocatalytic activity showing high efficiency against Rh-B, BTB, MB, MO dye molecules when compared with Fe_3O_4 NPs, CS/Fe_3O_4 NCs. The Rh-B molecules were completely degraded within short time period (40 min) when compared to BTB, MB, MO dye molecules in the presence of Gr/CS/Fe_3O_4 NCs. CS and Gr present in the NCs could act as an adsorbent and dispersing agent as well as electron reservoir to trap electrons from Fe_3O_4 NPs due to exposure to visible light, possibly delaying the electron–hole pair recombination.

CRediT authorship contribution statement

Muthuchamy Maruthupandy: Investigation, Funding acquisition, Writing - original draft. **Thillaichidambaram Muneeswaran:** Investigation, Writing - original draft. **Muthusamy Anand:** Resources, Funding acquisition. **Franck Quero:** Resources, Funding acquisition, Supervision, Writing - review & editing.

Acknowledgements

M. M. and F. Q. acknowledge the financial support from FONDECYT (Chile) under the Postdoctoral Fellowship No. 3180128. Francisco Melo and Victor Carrasco are acknowledged for providing access to their Raman spectroscopy facility financed by CONICYT/FONDEQUIP Grant No. EQM130149. The authors extend their acknowledgements to the FONDEQUIP Grant No. EQM150101 for providing access to FE-SEM (CIEN-UC).

References

[1] R.E. Connon, J. Geist, I. Werner, Effect-based tools for monitoring and predicting the ecotoxicological effects of chemicals in the aquatic environment, Sensors 12 (2012) 12741–12771.
[2] S.O. Adio, M.H. Omar, M. Asif, T.A. Saleh, Arsenic and selenium removal from water using biosynthesized nanoscale zero-valent iron: a factorial design analysis, Process Saf. Environ. 107 (2017) 518–527.
[3] A.A. Basaleh, M.H. Al-Malack, T.A. Saleh, Methylene blue removal using polyamide-vermiculite nanocomposites: kinetics, equilibrium and thermodynamic study, J. Environ. Chem. Eng. 7 (2019), 103107.
[4] T.A. Saleh, I. Ali, Synthesis of polyamide grafted carbon microspheres for removal of rhodamine B dye and heavy metals, J. Environ. Chem. Eng. 6 (2018) 5361–5368.
[5] M. Mir, I.B. Tahirbegi, J.J. Valle-Delgado, X. Fernàndez-Busquets, J. Samitier, In vitro study of magnetite-amyloid β complex formation, Nanomed. Nanotechnol. 8 (2012) 974–980.
[6] J.M. Knipe, J.T. Peters, N.A. Peppas, Theranostic agents for intracellular gene delivery with spatiotemporal imaging, Nano Today 8 (2013) 21–38.
[7] N.P. Herring, S.H. Almahoudi, C.R. Olson, M.S. El-Shall, Enhanced photocatalytic activity of Zn-graphene nanocomposites prepared by microwave synthesis, J. Nanopart. Res. 14 (2012) 1–13.
[8] A.I.S. Neves, T.H. Bointon, L.V. Melo, S. Russo, I. de Schrijver, M.F. Craciun, H. Alves, Transparent conductive graphene textile fibers, Sci. Rep. 5 (2015) 9866.
[9] I. Barbolina, R. Woods, N. Lozano, K. Kostarelos, K.S. Novoselov, I.S. Roberts, Purity of graphene oxide determines its antibacterial activity, 2D Mat 3 (2016) 025025, https://doi.org/10.1088/2053-1583/3/2/025025.
[10] Z. Zhu, L. Garcia-Gancedo, A.J. Flewitt, H. Xie, S. Moussy, W.I. Milne, A critical review of glucose biosensors based on carbon nanomaterials: carbon nanotubes and graphene, Sensors 12 (2012) 5996–6022.
[11] J.-L. Li, B. Tang, B. Yuan, L. Sun, X.-G. Wang, A review of optical imaging and therapy using nanosized graphene and graphene oxide, Biomat 34 (2013) 9519–9534.
[12] E. Akbari, Z. Buntat, M.J. Kiani, A. Enzevaee, M. Khaledian, Analytical model of graphene-based biosensors for bacteria detection, Int. J. Environ. Anal. Chem. 95 (2015) 847–854.
[13] D.S. Spencer, A.S. Puranik, N.A. Peppas, Intelligent nanoparticles for advanced drug delivery in cancer treatment, Cur. Opin. Chem. Eng. 7 (2015) 84–92.
[14] N.V. Hoa, T.T. Khong, T.T.H. Quyen, T.S. Trung, One-step facile synthesis of mesoporous graphene/Fe_3O_4/chitosan nanocomposite and its adsorption capacity for a textile dye, J. Wat. Proc. Eng. 9 (2016) 170–178.
[15] X. Wang, Z. Liu, X. Ye, K. Hu, H. Zhong, X. Yuan, H. Xiong, Z. Guo, A facile one-pot method to two kinds of graphene oxide-based hydrogels with broad-spectrum antimicrobial properties, Chem. Eng. J. 260 (2015) 331–337.
[16] H.V. Tran, L.T. Bui, T.T. Dinh, D.H. Le, C.D. Huynh, A.X. Trinh, Graphene oxide/Fe_3O_4/chitosan nanocomposite: a recoverable and recyclable adsorbent for organic dyes removal. Application to methylene blue, Mater. Res. Express 4 (2017), 035701. https://doi.org/10.1088/2053-1591/aa6096.
[17] F.Y. Cheng, C.H. Su, Y.S. Yang, C.S. Yeh, C.Y. Tsai, C.L. Wu, M.T. Wu, D.B. Shieh, Characterization of aqueous dispersions of $Fe_{(3)}O_{(4)}$ nanoparticles and their biomedical applications, Biomat 26 (2005) 729–738.
[18] G.D. Moeser, K.A. Roach, W.H. Green, T. Alan Hatton, P.E. Laibinis, High-gradient magnetic separation of coated magnetic nanoparticles, AICHE J. 50 (2004) 2835–2848.
[19] M. Nagpal, P. Chaudhary, S. Wachasundar, A. Eltayib, A. Raihan, Management of recurrent rhegmatogenous retinal detachment, Ind. J. Ophthalmol. 66 (12) (2018) 1763–1771.
[20] H.H. Yang, S.Q. Zhang, X.L. Chen, Z.X. Zhuang, J.G. Xu, X.R. Wang, Magnetite-containing spherical silica nanoparticles for biocatalysis and bioseparations, Anal. Chem. 76 (2004) 1316–1321.
[21] I.J. Bruce, T. Sen, Surface modification of magnetic nanoparticles with alkoxysilanes and their application in magnetic bioseparations, Langmuir 19 (2005) 7029–7035.
[22] M.R. Ghazanfari, M. Kashefi, S.F. Shams, M.R. Jaafari, Perspective of Fe_3O_4 nanoparticles role in biomedical applications, Biochem. Res. Int. (2016), 7840161. https://doi.org/10.1155/2016/7840161.
[23] T. Javanbakht, S. Laurent, D. Stanicki, K.J. Wilkinson, Relating the surface properties of superparamagnetic iron oxide nanoparticles (SPIONs) to their bactericidal effect towards a biofilm of *Streptococcus mutans*, PLoS One 11 (2016), e0154445. https://doi.org/10.1371/journal.pone.0154445.
[24] G. Rena, C. Clancya, T.M. Tamer, B. Schaller, G.M. Walker, M.N. Collinsad, Cinnamyl O-amine functionalized chitosan as a new excipient in direct compressed tablets with improved drug delivery, Int. J. Biol. Macromol. 141 (2019) 936–946.
[25] A. Nithya, K. Jothivenkatachalam, S. Prabhu, K. Jeganathan, Chitosan based nanocomposite materials as photocatalyst – a review, Mat. Sci. Forum. 781 (2014) 79–94.
[26] V.L.E. Siong, K.M. Lee, J.C. Juan, C.W. Lai, X.H. Tai, C.S. Khe, Removal of methylene blue dye by solvothermally reduced graphene oxide: a metal-free adsorption and photodegradation method, RSC Adv. 9 (2019) 37686–37695.
[27] J. Preethi, M.H. Farzana, S. Meenakshi, Photo-reduction of Cr(VI) using chitosan supported zinc oxide materials, Int. J. Biol. Macromol. 104(Pt B) (2017) 1783–1793.
[28] S. Mahalingama, Y.-H. Ahn, Improved visible light photocatalytic activity of rGO–Fe_3O_4–NiO hybrid nanocomposites synthesized by in situ facile method for industrial wastewater treatment applications, New J. Chem. 42 (2018) 4372–4383.
[29] W.S. Hummers, R.E. Offeman, Preparation of graphitic oxide, J. American Chem. Soc. 80 (1958) 1339.
[30] Y.P. Yew, K. Shameli, M. Miyake, N. Kuwano, N.B.B.A. Khairudin, S.E.B. Mohamad, K.X. Lee, Green synthesis of magnetite (Fe_3O_4) nanoparticles using seaweed (*Kappaphycus alvarezii*) extract, Nanoscale Res. Lett. 11 (2016) 276.
[31] C.L.C. Carvalho, A.T.B. Silva, R.A.S. Luz, G.M.B. Castro, C.L. Lima, V.R. Mastelaro, R.R. Silva, O.N. Oliveira, W. Cantanhedê, Development of $Co_3[Co(CN)_6]2/Fe_3O_4$ bifunctional nanocomposite for clinical sensor applications, ACS App. Nanomat. 1 (2018) 4283–4293.
[32] V. Mourya, N.N. Inamdar, Chitosan-modifications and applications: opportunities galore, React. Funct. Polym. 68 (2008) 1013–1051.
[33] T.A. Saleh, M. Tuzen, A. Sarı, Polyamide magnetic palygorskite for the simultaneous removal of Hg(II) and methyl mercury; with factorial design analysis, J. Environ. Manag. 211 (2018) 323–333.
[34] E. Fukada, Piezoelectricity in polymers and biological materials, Ultrasonics 6 (1968) 229–234.
[35] L. Zhao, K. Ma, Z. Yang, Changes of water hydrogen bond network with different externalities, Int. J. Mol. Sci. 16 (2015) 8454–8489.
[36] T. Mondal, P. Butler, R. Ashkar, A.K. Bhowmick, R. Krishnamoorti, Graphene nanocomposites with high molecular weight poly(ε-caprolactone) grafts: controlled synthesis and accelerated crystallization, ACS Macro Lett. 5 (2016) 278–282.
[37] T.A. Saleh, Naeemullah, M. Tuzen, A. Sarı, Polyethylenimine modified activated carbon as novel magnetic adsorbent for the removal of uranium from aqueous solution, Chem. Eng. Res. Des. 117 (2017) 218–227.
[38] S.-X. Wang, H. Maimaiti, B. Xu, A. Awati, G.-B. Zhou, Y.D. Cui, Synthesis and visible-light photocatalytic N2/H_2O to ammonia of ZnS nanoparticles supported by petroleum pitch-based graphene oxide, Appl. Surf. Sci. 493 (2019) 514–524.
[39] A.M. Atta, H.A. Al-Lohedan, S.A. Al-Hussain, Functionalization of magnetite nanoparticles as oil spill collector, Int. J. Molecul. Sci. 16 (4) (2015) 6911–6931.
[40] M. Sharafeldin, G.W. Bishop, S. Bhakta, A. El-Sawy, S.L. Suib, J.F. Rusling, Fe_3O_4 nanoparticles on graphene oxide sheets for isolation and ultrasensitive amperometric detection of cancer biomarker proteins, Biosens. Bioelectron. 91 (2017) 359–366.
[41] B. Bai, X. Xu, C. Li, J. Xing, H. Wang, Y. Suo, Magnetic Fe_3O_4@chitosan carbon microbeads: removal of doxycycline from aqueous solutions through a fixed bed via sequential adsorption and heterogeneous Fenton-like regeneration, J. Nanomat. (2018), 5296410. https://doi.org/10.1155/2018/5296410.
[42] T.A. Saleh, Simultaneous adsorptive desulfurization of diesel fuel over bimetallic nanoparticles loaded on activated carbon, J. Clean. Prod. 172 (2018) 2123–2132.
[43] T.A. Saleh, Nanocomposite of carbon nanotubes/silica nanoparticles and their use for adsorption of Pb(II): from surface properties to sorption mechanism, Desalin. Water Treat. 57 (2016) 10730–10744.
[44] D. Hou, Q. Liu, X. Wang, Y. Quan, Z. Qiao, L. Yu, S. Ding, Facile synthesis of graphene via reduction of graphene oxide by artemisinin in ethanol, J. Mater. 4 (2018) 256–265.
[45] G. Rajivgandhi, M. Maruthupandy, T. Veeramani, F. Quero, W.-J. Li, Anti-ESBL investigation of chitosan/silver nanocomposites against carbapenem resistant *Pseudomonas aeruginosa*, Int. J. Biol. Macromol. 132 (2019) 1221–1234.
[46] M. Mahdavi, M.B. Ahmad, M.J. Haron, F. Namvar, B. Nadi, M.Z.A. Rahman, J. Amin, Synthesis, surface modification and characterisation of biocompatible magnetic iron oxide nanoparticles for biomedical applications, Molecules 18 (2013) 7533–7548.
[47] I.O. Aladea, M.A.A. Rahman, T.A. Saleh, Modeling and prediction of the specific heat capacity of Al/water nanofluids using hybrid genetic algorithm/support vector regression model, Nano-Structures & Nano-Objects 17 (2019) 103–111.
[48] T.A. Saleh, Mercury sorption by silica/carbon nanotubes and silica/activated carbon: a comparison study, J. Water Supply Res. T. 6 (2015) 892–903.
[49] T.A. Saleh, Isotherm, kinetic, and thermodynamic studies on Hg(II) adsorption from aqueous solution by silica-multiwall carbon nanotubes, Environ. Sci. Pollut. Res. Int. 22 (2015) 16721–16731.
[50] L. Bokobza, J.-L. Bruneel, M. Couzi, Raman spectra of carbon-based materials (from graphite to carbon black) and of some silicone composites, Carbon 1 (1) (2015) 77–94.
[51] Y. Lin, X. Sun, D.S. Su, G. Centi, S. Perathoner, Catalysis by hybrid sp2/sp3 nanodiamonds and their role in the design of advanced nanocarbon materials, Chem. Soc. Rev. 47 (2018) 8438.
[52] R. Hufschmid, H. Arami, R.M. Ferguson, M. Gonzales, E. Teeman, L.N. Brush, N.D. Browning, K.M. Krishnana, Synthesis of phase-pure and monodisperse iron oxide nanoparticles by thermal decomposition, Nanoscale 7 (2015) 11142–11154.
[53] T. Peik-See, A. Pandikumar, H. Nay-Ming, L. Hong-Ngee, Y. Sulaiman, Simultaneous electrochemical detection of dopamine and ascorbic acid using an iron oxide/reduced graphene oxide modified glassy carbon electrode, Sensors 14 (2014) 15227–15243.
[54] A.R. Chowdhuri, T. Singh, S.K. Ghosh, S.K. Sahu, Carbon dots embedded magnetic nanoparticles @chitosan @metal organic framework as a nanoprobe for pH sensitive targeted anticancer drug delivery, ACS Appl. Mat. Inter. 8 (2016) 16573–16583.
[55] C. Ma, K. Yang, L. Wang, X. Wang, Facile synthesis of reduced graphene oxide/Fe_3O_4 nanocomposite film, J. Appl. Biomat. Func. Mat. 15 (2017) S1–S6.

[56] F.M. Pesci, G. Wang, D.R. Klug, Y. Li, A.J. Cowan, Efficient suppression of electron–hole recombination in oxygen-deficient hydrogen-treated TiO_2 nanowires for photoelectrochemical water splitting, J. Phy. Chem. C 117 (2013) 25837–25844.
[57] H. Hosseinzadeh, S. Hosseinzadeh, S. Pashaei, Fabrication of novel magnetic graphene oxide nanocomposites for selective adsorption of mercury from aqueous solutions, Environ. Sci. Pollut. Res. Int. 26 (2019) 26807–26821.
[58] S. Joshi, V.K. Garg, N. Kataria, K. Kadirvelu, Applications of Fe_3O_4@AC nanoparticles for dye removal from simulated wastewater, Chemosphere 236 (2019) 124280, https://doi.org/10.1016/j.chemosphere.2019.07.011.
[59] P. Mishra, S. Patnaika, K. Parida, An overview of recent progress on noble metal modified magnetic Fe_3O_4 for photocatalytic pollutant degradation and H_2 evolution, Catal. Sci. Technol. 9 (2019) 916–941.
[60] P.K. Koochana, A. Mohanty, B. Subhadarshanee, S. Satpati, R. Naskar, A. Dixitc, R.K. Behera, Phenothiazines and phenoxazines: as electron transfer mediators for ferritin iron release, Dalton Trans. 48 (2019) 3314–3326.
[61] S. Phanichphant, A. Nakaruk, K. Chansaenpak, D. Channei, Evaluating the photocatalytic efficiency of the BiVO4/rGO photocatalyst, Sci. Rep. 9 (2019), 16091. https://doi.org/10.1038/s41598-019-52589-5.
[62] W. Wang, Q. He, K. Xiao, L. Zhu, Electrostatic self-assembly of Fe_3O_4/GO nanocomposites and their application as an efficient Fenton-like catalyst for degradation of rhodamine B, Mat. Res. Exp. 5 (2018) https://doi.org/10.1088/2053-1591/aab2dc/meta.
[63] P.K. Boruah, P. Borthakur, G. Darabdhara, C.K. Kamaja, I. Karbhal, M.V. Shelke, et al., Sunlight assisted degradation of dye molecules and reduction of toxic Cr(VI) in aqueous medium using magnetically recoverable Fe_3O_4/reduced graphene oxide nanocomposite, RSC Adv. 6 (2016) 11049–11063.